








# Unusual Abundances from Planetary System Material Polluting the White Dwarf G238-44

Ted M Johnson<sup>1</sup> , Beth L. Klein<sup>1</sup> , D. Koester<sup>2</sup> , Carl Melis<sup>3</sup> , B. Zuckerman<sup>1</sup> , and M. Jura<sup>1,4</sup>

<sup>1</sup> Department of Physics and Astronomy, University of California, Los Angeles, CA 90095-1562, USA; [tedjohnson12@g.ucla.edu](mailto:tedjohnson12@g.ucla.edu)

<sup>2</sup> Institut für Theoretische Physik und Astrophysik, University of Kiel, D-24098 Kiel, Germany

<sup>3</sup> Center for Astrophysics and Space Sciences, University of California, San Diego, CA 92093-0424, USA

Received 2022 June 15; revised 2022 September 16; accepted 2022 November 3; published 2022 December 15

## Abstract

Ultraviolet and optical spectra of the hydrogen-dominated atmosphere white dwarf star G238-44 obtained with FUSE, Keck/HIRES, HST/COS, and HST/STIS reveal 10 elements heavier than helium: C, N, O, Mg, Al, Si, P, S, Ca, and Fe. G238-44 is only the third white dwarf with nitrogen detected in its atmosphere from polluting planetary system material. Keck/HIRES data taken on 11 nights over 24 yr show no evidence for variation in the equivalent width of measured absorption lines, suggesting stable and continuous accretion from a circumstellar reservoir. From measured abundances and limits on other elements, we find an anomalous abundance pattern and evidence for the presence of metallic iron. If the pollution is from a single parent body, then it would have no known counterpart within the solar system. If we allow for two distinct parent bodies, then we can reproduce the observed abundances with a mix of iron-rich Mercury-like material and an analog of an icy Kuiper Belt object with a respective mass ratio of 1.7:1. Such compositionally disparate objects would provide chemical evidence for both rocky and icy bodies in an exoplanetary system and would be indicative of a planetary system so strongly perturbed that G238-44 is able to capture both asteroid and Kuiper Belt–analog bodies near-simultaneously within its <100 Myr cooling age.

*Unified Astronomy Thesaurus concepts:* [Exoplanet systems \(484\)](#); [Stellar abundances \(1577\)](#); [White dwarf stars \(1799\)](#); [Planetary dynamics \(2173\)](#)

## 1. Introduction

It is now well-established that single white dwarf (WD) stars with  $T_{\text{eff}} \lesssim 25,000$  K whose spectra show absorption features from elements heavier than helium (high-Z) have accreted material from their extant planetary systems (e.g., Jura & Young 2014; Farihi 2016; Zuckerman & Young 2018; Veras 2021, and references therein). Perturbed planet(esimal) s in these evolved planetary systems (Debes & Sigurdsson 2002) will be tidally disrupted if they venture within the WD Roche radius, forming an accretion disk that “pollutes” the otherwise pure hydrogen and/or helium atmosphere of the WD star (Jura 2003). Measuring abundances of high-Z elements in these WD atmospheres has proved to be a unique and powerful method to determine the compositions of exoplanetary bodies to a high degree of precision and sensitivity.

For the most part, parent body compositions have been found to be consistent with dry, volatile-poor rocky material typical of the inner solar system (e.g., Jura 2006; Jura & Xu 2012; Wilson et al. 2016; Doyle et al. 2019). However, examples exist of objects very rich in water ice (e.g., Farihi et al. 2013; Raddi et al. 2015; Gänsicke et al. 2019; Doyle et al. 2021; Klein et al. 2021), including an exo-Kuiper Belt analog (Xu et al. 2017) and bodies massive enough to have experienced igneous differentiation into cores (Melis et al. 2011; Gänsicke et al. 2012) and crusts (Zuckerman et al. 2011; Melis & Dufour 2017). Even with this assortment of measured

exoplanetary compositions, it has consistently been the case that polluted white dwarf abundances can be reasonably fit with the compositions of known solar system bodies.

Theoretical works allow for pollution from multiple parent bodies (e.g., Jura 2008; Turner & Wyatt 2020), but to date all previously published polluted white dwarf systems are understood as accreting a single parent body. As we report herein, G238-44 appears to break the mold of past polluted white dwarf results. Either it is accreting material that is so alien as to have no known counterpart within the solar system, or it is simultaneously accreting from two compositionally distinct parent bodies.

G238-44 (13:38:50.47 +70:17:07.64; commonly used alternate names are EG 102 and WD1337+705) is a warm (effective temperature  $\approx 20,000$  K), hydrogen-dominated and metal-polluted atmosphere WD (spectral type DAZ). G238-44 was identified almost 80 yr ago by Kuiper (1942) when there were fewer than 80 WDs known (Luyten 1945). The proximity of G238-44 to Earth leads it to be quite bright for a WD at  $\approx 12^{\text{th}}$  mag, and combined with its relatively simple spectrum dominated by hydrogen Balmer lines (Figure 1), has seen the star extensively observed as both a spectrophotometric calibrator and a science object.

Absorption features of Si, C, and Al from International Ultraviolet Explorer (IUE) spectra provided the first evidence for elements other than H in the atmosphere of G238-44. This prompted debate about whether the ground-state and weakly excited ultraviolet (UV) lines were photospheric, interstellar, or circumstellar in origin (Vennes et al. 1991; Holberg et al. 1997, 1998). On the other hand, Mg II 4481 Å—arising from an excited state of 8.86 eV—is always photospheric, and its detection in G238-44 (Holberg et al. 1997) was the first observation of Mg in a DA of this temperature class. Radiative

<sup>4</sup> deceased.

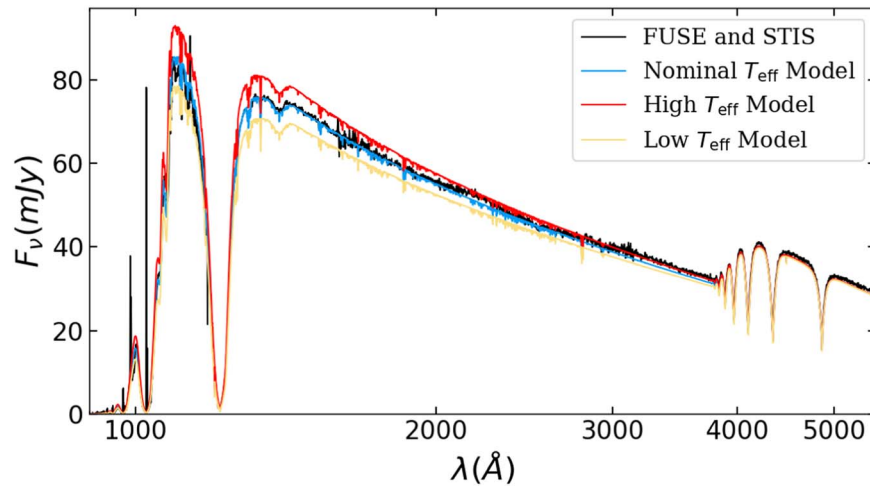


**Figure 1.** Ultraviolet and blue-optical spectra of G238-44 and models as described in Section 3.1. Low-resolution and high-S/N STIS spectra are displayed for wavelengths longer than 1300 Å in preference to lower-S/N COS spectra; STIS spectra are used as obtained from MAST without further processing. The model produced with nominal values of  $T_{\text{eff}}$  and  $\log g$  is an excellent match to the flux-calibrated spectra.

levitation can support high-Z elements (particularly Si, C, and Al) against gravitational settling in WD atmospheres, but the effect was shown to be negligible for Mg at  $T_{\text{eff}} \sim 20,000$  K (Chayer et al. 1995). Given that the settling timescales for high-Z elements are on the order of  $\sim$ days for G238-44, the Mg detection was early evidence that observed atmospheric pollution in this class of WDs must be associated with current and ongoing accretion.

Spitzer Infrared Array Camera 4.5 and 7.9  $\mu\text{m}$  photometry of G238-44 shows no infrared excess from any putative circumstellar disk at those wavelengths (Mullally et al. 2007). Farihi et al. (2009) report the detection of a faint MIPS 24  $\mu\text{m}$  source near G238-44’s location, which would suggest a subtle excess from cool ( $T < 400\text{K}$ ) dust if it is actually associated with the WD. However, the authors conclude that the potential for source confusion is high,  $\sim 25\%–70\%$ , and that the 24  $\mu\text{m}$  flux may not originate from G238-44. Thus, despite ongoing accretion, the debris reservoir around this star is among the vast majority that go undetected (Jura 2008; Rocchetto et al. 2015; Wilson et al. 2019b).

Optical detection of Ca was reported by Zuckerman & Reid (1998) and Zuckerman et al. (2003) as part of a larger study of WD pollution that concluded neither accretion of material from the interstellar medium (ISM) nor exo-comets can easily explain the observations. Subsequently, a suite of elements—C, N, O, Si, S, and Fe—detected in spectra from the Far Ultraviolet Spectroscopic Explorer (FUSE) were analyzed in the context of radiative levitation by Dupuis et al. (2007, 2010). They concluded that ongoing accretion, rather than radiative support of material from a past pollution event, must be responsible for the observed atmospheric pollution in this warm DAZ.

G238-44 earns the distinction of being one of just three known WDs to be polluted by planetary system material that produces detectable N absorption; the other two are G200-39 (Xu et al. 2017) and GD 378 (Klein et al. 2021). The detection of N is significant because it is typically indicative of exoplanetary ices or primitive volatile-rich material such as giant planets, Kuiper Belt–analog objects, and comet-like bodies.

In this paper, we collate data from a variety of UV and optical spectrographs (Section 2) to identify, characterize, and

measure 94 photospheric absorption lines in the spectrum of G238-44 (Section 3). Section 4 derives accretion rates for 10 high-Z elements and demonstrates that these elements are present in ratios unlike those of any known single solar system body. We put forward a model for pollution by two compositionally distinct parent bodies and show it provides a reasonable fit to the available data.

## 2. Observations

High-resolution spectra of G238-44 were obtained from various space telescope archives and our own observations with Keck/HIRES. An observing log appears in Table 1. Through this complementary combination of facilities and instruments, we cover a wide range of wavelengths and are able to compile the suite of elements presented in this study.

### 2.1. FUSE

G238-44 was observed in TTAG mode with the LWRS aperture of FUSE (Moos et al. 2000) on 2001 May 5 (PI J. Holberg) and again on 2002 January 27 (PI S. Friedman). While the wavelength range extended down to 905 Å, the flux for G238-44 is essentially zero for wavelengths shorter than 955 Å. These data were first published by Hébrard et al. (2003), who examined Lyman series quasi-molecular satellite features, and were revisited by Dupuis et al. (2007, 2010) and Barstow et al. (2014) in the context of high-Z abundances and radiative levitation.

Each observation included the four optical path channels (LiF1, LiF2, SiC1, and SiC2) focused on two detector segments (A and B), which resulted in eight independent spectra with varying degrees of overlap in wavelength coverage. For most of our analysis, we use a fully combined total spectrum provided by K. Long and B. Gänsicke (2012, private communication). We found that some unusual features appear in the region of the O I  $\lambda 1152$  line, which is covered by two of the eight channels/segments (LiF1B and LiF2A). To investigate the possible cause, we downloaded the uncombined data products available through the Mikulski Archive for Space Telescopes (MAST). We inspected the individual spectra as well as the nighttime-only versions of both epochs of observations, finding that the O I  $\lambda 1152$  feature has

**Table 1**  
Log of Observations

UT Date	Instrument	$\lambda$ Range (Å)	Exposure (s)	$R$	Program ID	P.I.
1997 Jul 07	HIRES Blue	3760–5250	1800	34,000	C08H	N. Reid
1998 Jan 23	HIRES Blue	3760–5250	900	34,000	U04H	B. Zuckerman
1999 Apr 20	HIRES Blue	3760–5250	2400	34,000	U06H	B. Zuckerman
1999 Jul 02	HIRES Red	4180–6710	3600	25,000	C04H	N. Reid
1999 Jul 03	HIRES Red	4180–6710	900	25,000	C04H	N. Reid
2001 May 05	FUSE	905–1180	10746	15,000	B119	J. Holberg
2002 Jan 27	FUSE	905–1180	17410	15,000	S601	S. Friedman
2006 Jun 11	HIRES Red	5560–10160	7200	37,000	U106Hr	B. Hansen
2006 Jun 17	HIRES Blue	3050–5940	3600	37,000	U106Hr	B. Hansen
2007 May 05	HIRES Blue	3050–5940	1800	37,000	U103Hb	B. Hansen
2007 May 06	HIRES Blue	3050–5940	3600	37,000	U103Hb	B. Hansen
2009 Dec 26	STIS E230H	2577–2835	1200	114,000	11568	S. Redfield
2009–2021	COS G185M	1730–1970	770	20,000		<i>Various</i>
2013–2017	COS G160M	1430–1800	301	20,000	<i>Various</i>	S. Penton
2016 Jun 03	HIRES Blue	3150–5940	1800	37,000	N171Hb	S. Redfield
2021 Dec 13	HIRES Blue	3050–5940	2000	37,000	U128Hb	C. Melis

**Notes.** COS spectra are from many observations combined. See Section 2.4.

contamination/distortions in the LiF2A spectra from both epochs (also in the night-only data), while the LiF1B spectra from both epochs look “normal.” We thus created an uncontaminated version of the 1100–1180 Å region by selecting only the LiF1B segments from both epochs.

We also found the multiplet of N II lines around 1084 Å to be unusually broad in the fully combined spectrum. Inspection of the individual segments revealed that the N II lines in the SiC1A segment of the S601 exposure were distorted (broader and shallower) compared to their appearance in the other three segments (SiC1A and SiC2B of B119 and SiC2B of S601). Thus, for the region of 1080–1090 Å, we created a combined spectrum omitting the S601–SiC1A segment. Since this was done outside of the CalFUSE pipeline, we do not report radial velocities for these lines.

The majority of detected absorption lines are found in these FUSE spectra, in which we identify transitions from C, N, O, Si, P, S, and Fe.

## 2.2. HIRES

Throughout the time span of 1997–2021, G238-44 was observed on 11 nights with the High Resolution Echelle Spectrograph (HIRES; Vogt et al. 1994) at the W. M. Keck Observatory (see Table 1). All observations reported used the C5 decker (mapping to a  $\approx 1''.15$  slit) and used either the red- or blue-optimized collimator. The 1997–1999 HIRES data were acquired with the pre-2004 single-CCD detector setup and were published by Zuckerman & Reid (1998) and Zuckerman et al. (2003). All subsequent data were taken using the updated three-detector mosaic, which resulted in improved resolution, wavelength coverage, and signal-to-noise ratio (S/N) compared to the older spectra.

Data were reduced with either PyRAF (Science Software Branch at STScI 2012) or the MAuna Kea Echelle Extraction (MAKEE<sup>5</sup>) pipeline and subsequently processed with methods following Klein et al. (2010). The spectra were continuum normalized by fitting low-order cubic spline functions and combined using PyRAF. Relatively long integrations obtained

in 2006–2007 resulted in an exceedingly high-quality spectrum with S/N per pixel of 190 near 3200 Å 370 near 3930 Å 220 near 4500 Å and 260 near 6350 Å. The high resolution and high S/N of these data enable the detection of lines with equivalent widths on the order of a few mÅ and allow us to report new optical detections of Si and Fe (previously seen Mg and Ca are also recovered).

## 2.3. STIS

G238-44 was observed by the Space Telescope Imaging Spectrograph<sup>6</sup> (STIS) aboard the Hubble Space Telescope (HST) on 2009 December 26 using the 0.2X0.2 aperture and E230H grating. The resulting spectrum has an S/N per pixel of 5. These data were published by Malamut et al. (2014) in an analysis using the ground-state near-UV Mg and Fe lines to study the local interstellar medium. In our reanalysis of this spectrum, we find that the origin of the Mg and Fe lines is almost entirely, if not completely, due to photospheric absorption (see Sections 3.4.4 and 3.4.10).

## 2.4. COS

These HST data were taken for the purpose of calibrating wavelength sensitivity and offsets. Between 2013 November 1 and 2017 September 6, G238-44 was observed 13 times with the HST Cosmic Origins Spectrograph<sup>7</sup> (COS) using the Primary Science Aperture (PSA) and G160M grating (Program IDs 13124, 13526, 13972, 14440, and 14857). When combined, the spectra provide an S/N per resolution element of 15.

G238-44 was also observed by COS using PSA and the G185M grating 11 times between 2009 July 21 and 2021 January 2 (Program IDs 11479, PI A. Aloisi; 13124, 13526, 13972, 14440, 14857, and 15389, PI S. Penton; 15542 and 15780, PI D. Sahnou). The 11 exposures have similar spectral resolutions and S/Ns, but they cover different wavelength regions. The spectra were combined to increase S/N in

<sup>5</sup> <https://www.astro.caltech.edu/~tb/makee/>

<sup>6</sup> <https://hst-docs.stsci.edu/stisihb>

<sup>7</sup> <https://hst-docs.stsci.edu/cosihb>

**Table 2**  
Summary of Parameters

$G$ (mag)	12.78 (0.01)
Distance (pc)	26.5 (0.2)
$T_{\text{eff}}$ (K)	20546 (474)
$\log g$	7.95 (0.03)
$M_{\text{WD}}(M_{\odot})$	0.597 (0.018)
$R_{\text{WD}}(R_{\odot})$	0.0136 (0.0003)
Cooling age (Myr)	50 (2)
$\dot{M}$ ( $\text{g s}^{-1}$ )	$5.8 \times 10^7$
Grav. redshift ( $\text{km s}^{-1}$ )	27.9 (1.5)
$V_{\text{r, helio}}$ ( $\text{km s}^{-1}$ )	1 (2)
$V_{\text{systemic}}$ ( $\text{km s}^{-1}$ )	-27 (3)

**Notes.**  $G$  magnitude and distance are from Gaia DR2 and EDR3.  $M_{\text{WD}}$ ,  $R_{\text{WD}}$ , gravitational redshift, and cooling age are from the Montreal White Dwarf Database (MWDD; Dufour et al. 2017) (<http://dev.montrealwhitedwarfdatabase.org/evolution.html>). Uncertainties given in parentheses represent the range in values for each parameter considered at the upper and lower limits of the  $T_{\text{eff}}/\log g$  models.  $\dot{M}$  is the total mass flow rate (see Section 4).

overlapping spectral regions, resulting in an S/N per resolution element around 1862 Å of  $\approx 20$ .

We identify absorption lines from Al II and Al III in the combined COS spectra.

### 3. Models and Measurements

#### 3.1. Stellar Parameters

White dwarf model atmospheres and synthetic spectra used in this work are described in Koester (2010). We fit a pure hydrogen atmosphere model to the G238-44 Gaia DR2 photometry and parallax to obtain the atmospheric parameters listed in Table 2. The initial fit suggested a  $T_{\text{eff}}$  error of 101 K and resulted in a reduced  $\chi^2$  of 22. This fit utilized unrealistically small magnitude errors from the Gaia DR2 catalog. Thus, errors on the photometry were scaled up by a multiplicative factor until we obtained a final best-fit  $\chi^2 \sim 1$ .

Figure 1 shows flux-calibrated UV and optical spectra overlaid with our models at the lower, nominal, and upper limits of  $T_{\text{eff}}/\log g$  solutions. The excellent match of the nominal model to the flux-calibrated spectra adds confidence that these stellar parameters indeed provide an accurate description of the available data for G238-44, especially given that, at a distance of only 26.5 pc we do not expect reddening to affect the UV fluxes. We note that GALEX FUV and NUV photometric measurements of G238-44 are available, but its brightness puts it in the nonlinear regime of the instrument, where the GALEX magnitudes are clearly affected according to the known linearity response plot.<sup>8</sup>

#### 3.2. Metal Absorption Lines

Table 3 presents a line list for the 94 absorption lines from heavy elements we identified in the collected spectroscopic data sets. Each line was matched to an atomic transition using the Vienna Atomic Line Database (VALD<sup>9</sup>) and/or the National Institute of Standards and Technology (NIST<sup>10</sup>)

**Table 3**  
Absorption Line List

$\lambda_{\text{lab}}$ (Å)	Species	$V_r$ ( $\text{km s}^{-1}$ )	EW (mÅ)	$\chi$ (eV)	$\log(gf)$
1009.858	C II	2.7	$16.7 \pm 5.0$	5.332	-0.462
1010.083	C II	0.9	$25.9 \pm 7.2$	5.334	-0.161
1010.371	C II	1.0	$24.1 \pm 5.5$	5.338	0.015
1036.337	C II	-3.0	$95.8 \pm 22.8$	0.000	-0.624
1037.018	C II	-3.6	$110.7 \pm 19.7$	0.008	-0.328
1065.891	C II	-5.6	$28.9 \pm 3.2$	9.290	-0.052
1066.133	C II	0.8	$25.3 \pm 3.5$	9.290	-0.307
1174.933	C III	-0.8	$24.2 \pm 5.1$	6.496	-0.468
1175.263	C III	-2.5	$25.6 \pm 5.4$	6.493	-0.565
1175.6	C III		$85.1 \pm 14.3$	6.496	-0.690
				6.503	0.009
1175.987	C III	0.8	$16.5 \pm 4.5$	6.496	-0.565
1176.370	C III	0.0	$16.2 \pm 4.7$	6.503	-0.468
1083.990	N II	0.0	$47.5 \pm 4.5$	0.000	-0.939
1084.580	N II	0.0	$60.8 \pm 4.3$	0.006	-0.587
1085.546	N II	0.0	$40.2 \pm 4.7$	0.016	-1.078
1085.700	N II	0.0	$55.7 \pm 4.4$	0.016	-0.320
1152.150	O I	0.0	$30.4 \pm 6.0$	1.967	-0.268
2791.600	Mg II	2.4	$81.2 \pm 25.9$	4.422	0.280
2796.352	Mg II	2.3	$226.3 \pm 38.1$	0.000	0.100
2798.823	Mg II	0.0	$95.8 \pm 21.4$	4.434	0.530
2803.531	Mg II	1.5	$171.0 \pm 21.6$	0.000	-0.210
4481	Mg II		$95.3 \pm 23.1$	8.864	0.740
				8.864	-0.560
				8.864	0.590
1670.787	Al II	-3.5	$82.0 \pm 10.9$	0.000	0.263
1721	Al II		$25.7 \pm 7.1$	4.644	-0.170
				4.644	0.307
1724.982	Al II	-4.4	$73.4 \pm 12.3$	4.659	0.577
1854.716	Al III	0.0	$123.9 \pm 19.3$	0.000	0.060
1862.790	Al III	0.3	$87.3 \pm 21.3$	0.000	-0.240
992.683	Si II	3.5	$75.0 \pm 17.6$	0.036	-0.277
3856.019	Si II	0.6	$1.8 \pm 0.4$	6.859	-0.406
3862.595	Si II	0.4	$1.3 \pm 0.4$	6.858	-0.860
4128.054	Si II	1.2	$1.7 \pm 0.8$	9.837	0.359
4130.894	Si II	-0.5	$1.5 \pm 0.5$	9.839	0.552
6347.109	Si II	0.6	$10.8 \pm 1.5$	8.121	0.297
6371.370	Si II	1.5	$10.3 \pm 2.4$	8.121	-0.003
1108.358	Si III	-5.7	$67.3 \pm 3.5$	6.537	-0.056
1110	Si III		$116.9 \pm 3.3$	6.553	-0.186
				6.553	0.294
1113	Si III		$158.9 \pm 5.4$	6.585	-1.356
				6.585	-0.186
				6.585	0.564
1141.579	Si III	-0.8	$14.3 \pm 3.0$	16.098	0.470
1144.309	Si III	-8.1	$18.4 \pm 3.4$	16.131	0.740
1128.340	Si IV	-3.2	$12.2 \pm 1.9$	8.896	0.470
1153.995	P II	-12.2	$9.9 \pm 3.6$	0.058	-0.032
1124.395	S II	-8.4	$4.7 \pm 2.4$	3.041	-1.190
1124.986	S II	-4.6	$18.8 \pm 3.8$	3.047	-0.630
1131.059	S II	-4.0	$12.7 \pm 4.5$	3.041	-0.990
1131.657	S II	-5.6	$3.4 \pm 1.1$	3.047	-1.360
3158.869	Ca II	2.0	$8.5 \pm 0.9$	3.123	0.241
3179.331	Ca II	1.6	$4.3 \pm 1.2$	3.151	0.499
3736.902	Ca II	2.6	$0.9 \pm 0.3$	3.151	-0.173
3933.663	Ca II	0.5	$28.5 \pm 0.5$	0.000	0.105
3968.469	Ca II	0.3	$5.5 \pm 0.6$	0.000	-0.200
3349.402	Ti II		$< 0.7$	0.049	0.530
1004.670	Ti III		$< 7.2$	4.764	0.510
3132.053	Cr II		$< 1.3$	2.483	0.423
3441.987	Mn II		$< 0.3$	1.776	-0.360
1063.176	Fe II	-3.9	$11.5 \pm 5.0$	0.000	-0.262
1068.346	Fe II	-3.6	$20.9 \pm 3.4$	0.048	-0.662

<sup>8</sup> [https://asd.gsfc.nasa.gov/archive/galex/Documents/brightness\\_limits.html](https://asd.gsfc.nasa.gov/archive/galex/Documents/brightness_limits.html)

<sup>9</sup> <http://vald.astro.uu.se/>

<sup>10</sup> <https://www.nist.gov/pml/atomic-spectra-database>

**Table 3**  
(Continued)

$\lambda_{\text{lab}}$ (Å)	Species	$V_r$ (km s <sup>-1</sup> )	EW (mÅ)	$\chi$ (eV)	log( <i>gf</i> )
1096.607	Fe II	-8.2	8.5 ± 2.9	0.048	-0.790
1096.877	Fe II	-13.4	9.8 ± 3.2	0.000	-0.486
1121.975	Fe II	-6.2	11.5 ± 2.1	0.000	-0.538
1125.448	Fe II	-8.9	10.9 ± 4.0	0.000	-0.807
1145	Fe II		25.2 ± 3.1	0.000	0.037
				0.000	-0.081
1148.277	Fe II	-10.4	19.4 ± 3.7	0.048	-0.179
1151.146	Fe II	-7.4	10.1 ± 3.4	0.083	-0.451
2586.650	Fe II	2.0	22.7 ± 6.6	0.000	-1.490
2592.318	Fe II	2.7	28.9 ± 8.7	1.040	-0.504
2593.560	Fe II	1.0	29.3 ± 8.9	4.076	0.646
2599.147	Fe II	1.0	36.8 ± 7.6	0.048	-0.062
2600.173	Fe II	0.9	57.8 ± 11.5	0.000	0.384
2607.867	Fe II	1.3	35.7 ± 7.9	0.083	-0.132
2612.654	Fe II	2.1	39.5 ± 10.4	0.048	0.000
2614.605	Fe II	0.0	50.8 ± 10.9	0.107	-0.355
2626.451	Fe II	-0.3	30.5 ± 10.4	0.048	-0.468
2629.078	Fe II	-0.6	37.0 ± 7.9	0.121	-0.457
2631.833	Fe II	-0.6	31.5 ± 9.8	0.107	-0.304
2632.108	Fe II	2.1	26.4 ± 7.9	0.083	-0.306
2740.359	Fe II	2.7	51.4 ± 13.7	0.986	0.302
2744.009	Fe II	0.8	25.2 ± 7.3	1.097	-0.054
2747.296	Fe II	1.2	44.6 ± 12.8	1.076	0.151
2747.794	Fe II	0.9	40.5 ± 14.4	1.040	0.051
2750.134	Fe II	1.4	53.8 ± 14.7	1.040	0.294
2756.552	Fe II	1.0	58.8 ± 13.1	0.986	0.390
2768.321	Fe II	-0.2	25.0 ± 9.2	3.245	0.405
3213.309	Fe II	1.5	2.0 ± 0.3	1.695	-1.250
3227.742	Fe II	-0.2	3.6 ± 0.5	1.671	-0.960
5169.033	Fe II	0.6	3.0 ± 1.2	2.891	-1.000
1098.241	Fe III	-1.1	11.7 ± 2.7	6.250	-0.550
1122.524	Fe III	-6.1	52.4 ± 3.1	0.000	-0.156
1124.874	Fe III	-5.1	38.3 ± 4.9	0.054	-0.447
1126.723	Fe III	-3.3	29.5 ± 6.9	0.092	-0.875
1128.042	Fe III	-2.7	23.5 ± 2.2	0.054	-0.746
1128.718	Fe III	-4.5	33.1 ± 3.2	0.092	-0.653
1129.185	Fe III	-2.4	23.2 ± 2.8	0.116	-0.767
1130.397	Fe III	-4.0	16.7 ± 2.3	0.137	-1.120
1131.189	Fe III	-1.9	19.3 ± 7.0	0.116	-1.244
1131.908	Fe III	-2.4	9.5 ± 2.5	0.092	-1.594
1143.666	Fe III	-9.7	8.3 ± 5.6	3.809	-0.966
1140.459	Ni II		< 7.7	1.254	-0.494

**Notes.** Here,  $\lambda < 3000$  Å is given in vacuum, while  $\lambda \geq 3000$  Å is given in air. The atomic data are the values used in our models for this analysis. Features at 1175.6, 4481, 1721.3, 1110, 1113.2, and 1144.9 are blended lines, and the quoted EW is the sum of the blend.

Atomic Spectra Database. Both the lower energy level of the transition and the log(*gf*) were considered when determining the line identifications and their inclusion in the line list. We list the adopted laboratory wavelengths, lower energy levels, and oscillator strengths used for modeling lines in Table 3.

Equivalent widths (EWs) were measured by fitting Voigt profiles to absorption lines with IRAF’s *splot* routine. Uncertainties for each line were calculated by summation in quadrature of *splot*’s line-fitting uncertainties and the rms of (typically) three EW measurements where the continuum level was varied within the noise between each measurement. Line centers were measured either from the *splot* profile fitting or visual inspection of the line, from which we calculated

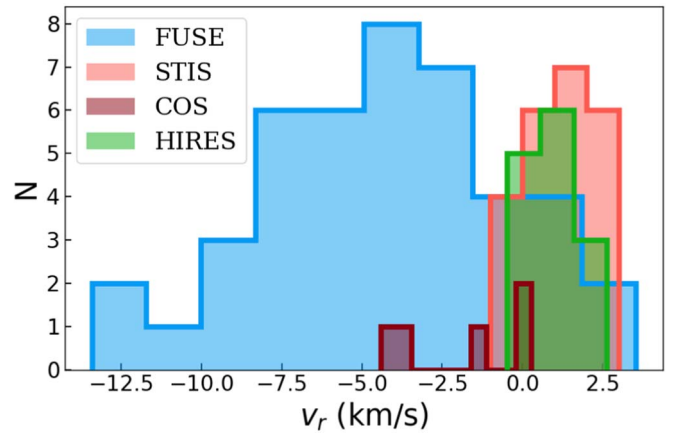


**Figure 2.** Distribution of heliocentric radial velocities measured for the absorption lines detected in spectra of G238-44. See also Section 3.2.

heliocentric radial velocities reported in Table 3 and displayed in Figure 2. In the case of a blended feature, e.g., Mg II 4481 Å, we use the sum of EWs resulting from fitting multiple profiles simultaneously with *splot*’s “deblending” routine and do not report radial velocity measurements.

While the measurements from the different instruments are in general agreement, the peak of the distribution of FUSE RVs is offset from HIRES and STIS by about  $-5$  km s<sup>-1</sup>, and it has a wider spread. This is consistent with the known absolute and relative wavelength calibration uncertainties of FUSE spectra (see FUSE Data Handbook<sup>11</sup>). From the 14 high-Z lines in the HIRES data, we find an average RV of  $0.9$  km s<sup>-1</sup> with a standard deviation of  $0.9$  km s<sup>-1</sup>. These are in agreement with H $\alpha$  and H $\beta$ , both of which have RVs of  $1$  km s<sup>-1</sup>. Adding in an absolute wavelength scale calibration uncertainty of  $\approx 1$  km s<sup>-1</sup>, we find a heliocentric RV (which includes the gravitational redshift component) for G238-44 of  $1 \pm 2$  km s<sup>-1</sup>.

Warm accreting WDs with short settling times would be expected to display variations in atmospheric pollution if there are variations in the accretion rate or inhomogeneities in the accretion–diffusion process, e.g., inefficient horizontal spreading of accreted material on the surface of the WD (Cunningham et al. 2021). However, robust evidence for atmospheric abundance variability in such systems has not yet been found (Debes & López-Morales 2008; Farihi et al. 2018; Wilson et al. 2019a). With settling times on the order of days and being bright enough to produce high-S/N high-resolution spectra, G238-44 is a prime candidate to monitor for changes in high-Z absorption lines over time.

Table 4 and Figure 3 show the EWs and profiles of Ca II K and Mg II 4481 Å in each epoch they have been observed with HIRES. With the exception of a single HIRES blue spectrum from 2016 (PI: S. Redfield), all observations result in equivalent widths and line profiles that, within the uncertainties, are consistent from one epoch to another. With just one inconsistent spectrum out of ten, we can only say that the 2016 measurement appears anomalous for some reason; as it stands, we are currently unable to provide a definitive explanation. We do not include the 2016 spectrum in any analysis, due to the unexplained low line EWs. A second epoch with a significant EW change would be required in order to convincingly argue

<sup>11</sup> [https://archive.stsci.edu/fuse/DH\\_Final/index.html](https://archive.stsci.edu/fuse/DH_Final/index.html)

**Table 4**  
HIRES Epoch EW Measurements

Date	Ca K (mÅ)	Mg II $\lambda$ 4481 (mÅ)
1997 Jul 07	27.1 $\pm$ 2.4	95.0 $\pm$ 8.7
1998 Jan 23	28.2 $\pm$ 1.7	99.1 $\pm$ 7.4
1999 Apr 20	25.8 $\pm$ 1.7	95.7 $\pm$ 10.8
1999 Jul 02	–	104.0 $\pm$ 6.9
1999 Jul 03	–	98.3 $\pm$ 11.8
2006 Jun 17	29.9 $\pm$ 2.1	109.3 $\pm$ 4.6
2007 May 05	29.3 $\pm$ 4.8	95.0 $\pm$ 13.6
2007 May 06	27.3 $\pm$ 2.4	100.9 $\pm$ 4.7
2016 Jun 03	22.6 $\pm$ 2.9	59.1 $\pm$ 12.3
2021 Dec 13	30.5 $\pm$ 2.9	93.5 $\pm$ 7.1

**Notes.** Lines were measured in the reduced spectra prior to being normalized and combined. Each measurement is an average of the multiple exposures and echelle orders from that epoch.

that this WD has displayed robust and meaningful line strength variations.

### 3.3. Abundances

For each absorption line, we calculate an elemental abundance by linearly scaling a model input abundance by the ratio of EW measured in the observed spectrum to that of the model. From the set of lines for each element, we take the average abundance (giving all lines equal weight) as the input abundance for the next model iteration. This process is repeated until the average abundance for each element converges, resulting in our final best-fit model. Abundances are reported in Table 5.

To derive uncertainties, we take into consideration the spread of abundances from lines of the same element (standard deviation of the mean; SDOM) and abundance changes from varying  $T_{\text{eff}}/\log g$ . In the case of elements with only one line detected, there is no SDOM; instead, the propagated line

measurement error is used. It has been shown, for helium-dominated WDs at least (Klein et al. 2010, 2011), that element-to-element abundance ratios are only weakly dependent on changes in atmospheric parameters  $T_{\text{eff}}/\log g$ . Similarly, for G238-44, we find relative abundances are much less sensitive to variations in the stellar parameters than are absolute abundances.

Fe, Si, and Mg display absorption lines in both UV and optical spectra for G238-44. We show in Table 6 the abundances calculated separately for the different instruments (and hence wavelength regimes). The Mg abundances are in excellent agreement, but there are discrepancies of  $\simeq 0.2$ – $0.3$  dex in the nominal abundances of Si and Fe derived from UV and optical lines, although they do agree within the uncertainties. We also see a trend with Si ionization state:  $\log(\text{Si}/\text{H}) = -6.36^{+0.13}_{-0.18}$ ,  $-6.66^{+0.05}_{-0.06}$ ,  $-7.04^{+0.08}_{-0.10}$  from Si II, Si III, and Si IV, respectively. We ran tests to see if different  $T_{\text{eff}}$  models could bring the abundances for these different ionization states into better agreement, but found only minimal improvement. UV-optical discrepancies have been noted before (e.g., Jura et al. 2012; Gänsicke et al. 2012; Wilson et al. 2019a; Xu et al. 2019). Gänsicke et al. (2012) provided an in-depth consideration of possible origins of the UV-optical discrepancies they found in warm H-dominated WDs similar to G238-44, including uncertain atomic data, abundance stratification, and genuine variation of accretion rates, but no clear culprit was identified. Section 3.2 suggests there are no obvious variations in the accretion rate for G238-44.

### 3.4. Individual Elements

Figures 4–6 show representative elemental absorption lines. More detailed discussion for each element appears below.

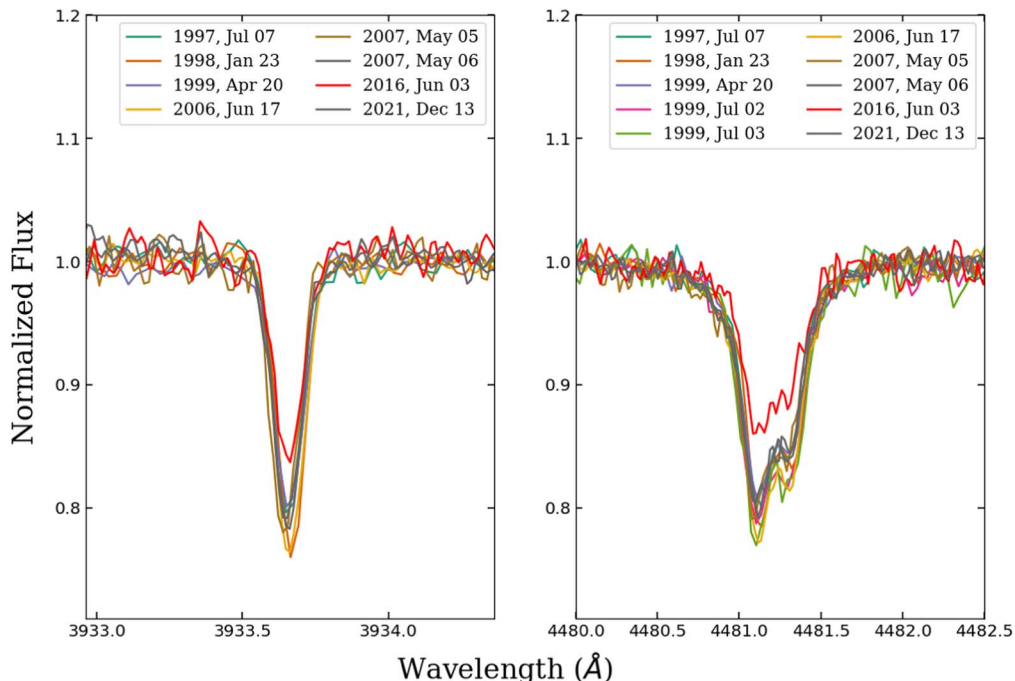


**Figure 3.** Multiple epochs of HIRES spectra showing Ca II K (left) and Mg II  $\lambda$ 4481 (right). With the exception of the anomalous 2016 epoch, the line strengths all look the same over the 24 yr period during which the spectra were obtained.

**Table 5**  
Accreting Material

at. #	Z	$n(Z)/n(H)$	$\log(n(Z)/n(H))$	$f_Z$ ( $10^6 \text{ g s}^{-1}$ )	$n(Z)/n(O)$	% by mass
6	C	$(1.02 \pm 0.27) \times 10^{-6}$	$-5.99_{-0.13}^{+0.10}$	$2.1 \pm 0.5$	$0.19 \pm 0.06$	$3.5 \pm 0.7$
7	N	$(1.47 \pm 0.30) \times 10^{-7}$	$-6.83_{-0.10}^{+0.08}$	$0.54 \pm 0.11$	$0.043 \pm 0.013$	$0.91 \pm 0.17$
8	O	$(2.73 \pm 0.58) \times 10^{-6}$	$-5.56_{-0.10}^{+0.08}$	$14.3 \pm 3.0$	–	$24.1 \pm 4.0$
12	Mg	$(2.17 \pm 0.54) \times 10^{-6}$	$-5.66_{-0.12}^{+0.10}$	$8.4 \pm 2.1$	$0.39 \pm 0.12$	$14.1 \pm 2.7$
13	Al	$(5.88 \pm 1.30) \times 10^{-8}$	$-7.23_{-0.11}^{+0.09}$	$0.27 \pm 0.06$	$0.0111 \pm 0.0034$	$0.452 \pm 0.086$
14	Si	$(3.99 \pm 1.36) \times 10^{-7}$	$-6.40_{-0.18}^{+0.13}$	$2.09 \pm 0.71$	$0.083 \pm 0.033$	$3.52 \pm 0.82$
15	P	$(7.43 \pm 2.85) \times 10^{-9}$	$-8.13_{-0.21}^{+0.14}$	$0.05 \pm 0.02$	$0.0018 \pm 0.0008$	$0.084 \pm 0.021$
16	S	$(1.72 \pm 0.72) \times 10^{-7}$	$-6.76_{-0.24}^{+0.15}$	$1.44 \pm 0.60$	$0.050 \pm 0.023$	$2.42 \pm 0.64$
20	Ca	$(1.78 \pm 0.39) \times 10^{-7}$	$-6.75_{-0.11}^{+0.09}$	$1.90 \pm 0.42$	$0.053 \pm 0.015$	$3.20 \pm 0.57$
22	Ti	$<(4.52) \times 10^{-8}$	$< -7.34$	$<0.6$	$<0.01$	$<1.1$
24	Cr	$<(3.07) \times 10^{-8}$	$< -7.51$	$<0.5$	$<0.01$	$<0.9$
25	Mn	$<(1.46) \times 10^{-8}$	$< -7.84$	$<0.3$	$<0.01$	$<0.5$
26	Fe	$(1.31 \pm 0.40) \times 10^{-6}$	$-5.88_{-0.16}^{+0.12}$	$26.6 \pm 8.2$	$0.53 \pm 0.19$	$44.8 \pm 4.7$
28	Ni	$<(2.18) \times 10^{-7}$	$< -6.66$	$<5.1$	$0.03 \pm 0.01^a$	$2.9 \pm 0.6^a$

**Notes.**  $n(Z)/n(H)$  are the observed atmospheric elemental abundances by number.  $f_Z$  is the diffusion flux calculated at optical depth  $\tau=1$ , assuming steady-state accretion.  $n(Z)/n(O)$  are calculated from  $f_Z$  and represent the ratios in the accreting material. The total diffusion flux of heavy elements through the atmosphere (and hence, total accretion rate) is  $(57.7 \pm 9.1) \times 10^6 \text{ g s}^{-1}$ .

<sup>a</sup> These values are set such that Ni/Fe is equal to that of a CI Chondrite.

**Table 6**  
UV versus Optical Abundances

Z	FUSE 905–1195 Å	STIS 1150–1750 Å	HIRES 3000–10000 Å
Z		$\log(Z/H)$	
Mg	–	$-5.66_{-0.12}^{+0.10}$	$-5.68_{-0.12}^{+0.10}$
Si	$-6.66_{-0.10}^{+0.08}$	–	$-6.36_{-0.29}^{+0.17}$
Fe	$-6.06_{-0.13}^{+0.10}$	$-5.76_{-0.16}^{+0.12}$	$-5.83_{-0.16}^{+0.12}$

### 3.4.1. Carbon

Absorption lines from C II and C III are present in FUSE spectra. The lines at 1036 and 1037 Å come from the ground state and a slightly excited state, respectively. All other C lines are from excited states and are photospheric. Figure 6 shows that the 1036 and 1037 Å lines are consistent with a model of purely photospheric absorption. Thus, any ISM component of their line strengths would have to be negligibly small and at the same radial velocity as the photospheric lines.

### 3.4.2. Nitrogen

All four N lines detected in the FUSE spectrum come from either the ground state or only slightly excited states (Table 3), therefore it is important to assess if they could originate in the ISM. In Table 7, we show a comparison of the relative N II line strengths for G238-44 to those of measured ISM lines toward the B1V star  $\alpha$  Virginis located 77 pc from Earth (York & Kinahan 1979). The  $\alpha$  Virginis measurements show that the ISM contribution to absorption in the excited states is significantly less, or absent, compared to the ground-state line. Our measured relative line strengths for all four N II lines observed in G238-44 are not consistent with the ISM measurements for  $\alpha$  Virginis. Given the relative observed line strengths, and the agreement with predicted model photospheric abundances for all N lines in G238-44, we conclude that the nitrogen detected in its spectrum is photospheric.

### 3.4.3. Oxygen

The O I 1152 Å line is detected in the FUSE spectrum. It is a clear, strong line that comes from an excited state and is not expected to contain any contribution from the ISM.

### 3.4.4. Magnesium

Mg is detected in the optical (blended) triplet at 4481 Å arising from an excited state of 8.9 eV. Four Mg II lines are detected in the near-UV around 2800 Å; two of these come from the ground state and two arise from excited levels of 4.4 eV. The excited state lines must be photospheric in origin, and our model provides consistent fits to both optical and UV excited lines. Figure 4 shows that the model based on photospheric absorption fits all four near-UV lines well, including the ground-state lines previously attributed to the ISM by Malamut et al. (2014). We conclude that the ground-state Mg II lines are almost completely, if not entirely, also photospheric in origin.

### 3.4.5. Aluminum

Six Al lines are found in the HST/COS data. Three of these arise out of the ground state, but the other three are from an excited state of 4.6 eV and are thus photospheric. Our model fits to the photospheric lines do not suggest an ISM contribution to the ground-state lines.

### 3.4.6. Silicon

Si II, III, and IV are found in FUSE data, and Si II lines are found in optical data. We identified a total of 16 transitions; essentially all of these lines come from excited states and are necessarily photospheric. Comparison of abundances derived from the sets of UV and optical Si lines indicates discrepancies that have been previously noted for polluted WDs. See Section 3.3 for more discussion.

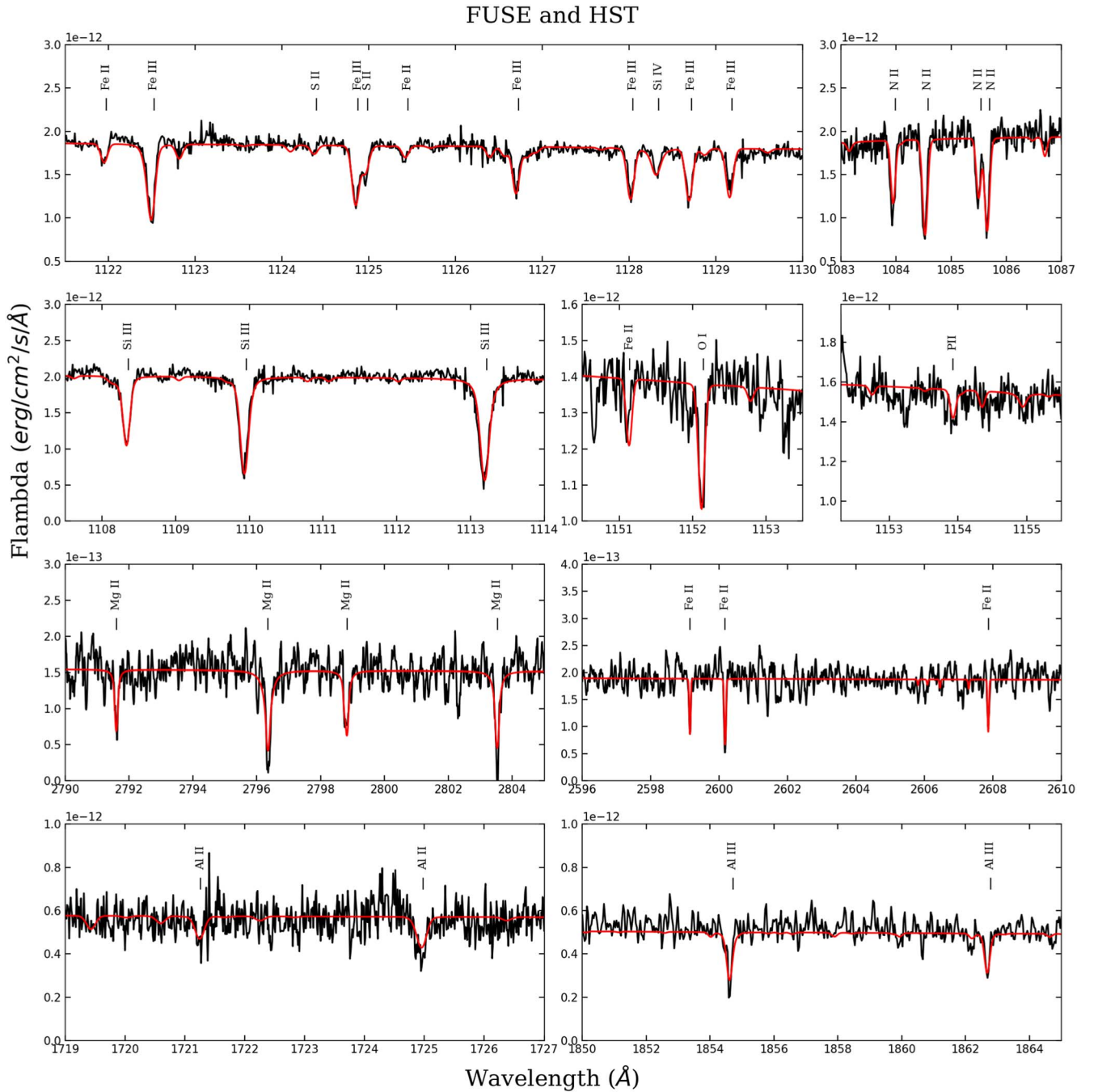


**Figure 4.** Select regions of FUSE and HST spectra; the model with the best-fit abundances is overplotted in red. The STIS spectrum (showing the 2800  $\text{\AA}$  Mg II lines and 2600  $\text{\AA}$  Fe II lines) has been smoothed with a 5 pixel boxcar function.

### 3.4.7. Phosphorus

The only phosphorus line observed is P II at 1153.995  $\text{\AA}$ ; we regard it as a marginal detection. This transition is slightly excited. York & Kinahan (1979) detected toward  $\alpha$  Virginis the ground-state P II line at 1152.818  $\text{\AA}$  from the ISM, but did not detect the 1153.995  $\text{\AA}$  line. Their study, with a resolution of 0.05  $\text{\AA}$ , had the resolving power to distinguish between the two lines. We do not detect P II absorption at 1152.818  $\text{\AA}$ , therefore any absorption from the excited state P II line at 1153.995  $\text{\AA}$  is not interstellar in origin. The potentially stronger P II line at 1015.46  $\text{\AA}$  seen in other polluted WDs (e.g., GD 378, Klein et al. 2021) is not detected in G238-44, which is unsurprising

as it lies on the blue wing of Lyman- $\beta$  where the S/N is only 7, as compared to an S/N of 25 near 1153.995  $\text{\AA}$ .

### 3.4.8. Sulfur

Four S II lines are detected in FUSE data. The lines come from excited states and are not from the ISM.

### 3.4.9. Calcium

Ca II is detected via five optical transitions. The weakest line detected in this study is the Ca II 3736  $\text{\AA}$  line with an equivalent width of  $0.89 \pm 0.27$  m $\text{\AA}$ . This is made possible by the high S/N of these data and the high resolving power of HIRES.

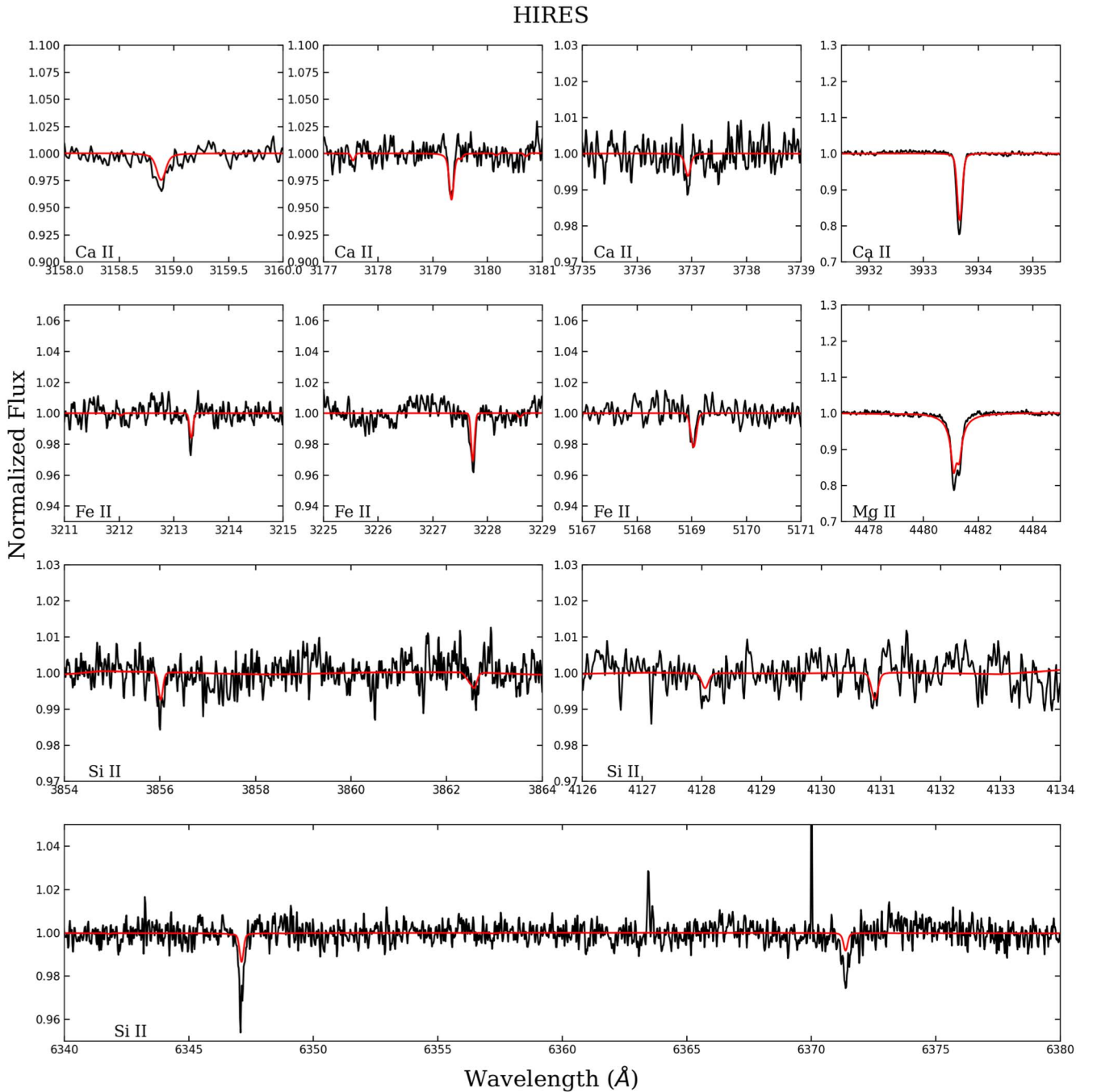


**Figure 5.** HIRES spectra showing all detected lines (except Ca II  $\lambda$ 3968 which lies within the H $\epsilon$  Balmer transition). The model with the best-fit abundances is overplotted in red.

#### 3.4.10. Iron

Many Fe II lines are detected in FUSE, STIS, and HIRES data; Fe III is also seen in the FUSE spectrum. Similar to the situation with Mg II STIS lines (Section 3.4.4), the ground-state Fe II lines are well-fit by our model at the derived photospheric abundance and do not reveal any significant contribution from the ISM.

#### 3.4.11. Titanium, Chromium, Manganese, and Nickel

We measure upper limits for Ti, Cr, Mn, and Ni. These were determined by adjusting the abundance of these elements in the

model until the absorption was comparable to the noise in their region of the HIRES spectrum.

## 4. Discussion

Metals in the atmosphere of G238-44 should settle out of view within timescales on the order of days (Koester 2009). Combined with an essentially stable atmospheric pollution level detected over decades, we conclude that G238-44 is in a steady-state accretion phase (meaning the inflow of material is balanced by losses due to settling). This is assumed to be the case for all further analysis wherein atmospheric abundances are mapped to parent body compositions. Following Gänsicke

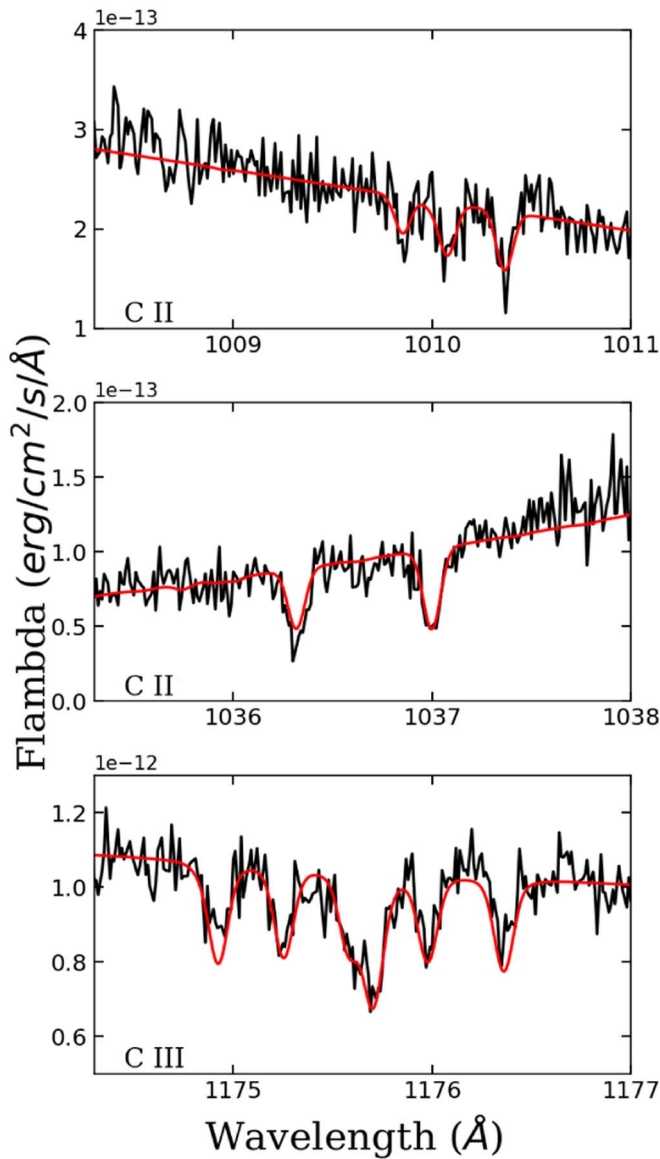


Figure 6. Carbon lines found in FUSE spectra. See Section 3.4.1.

Table 7  
N II EWs for  $\alpha$  Virginis and G238-44

$\lambda$ (Å)	Eq. Width (mÅ)		$\chi$ (eV)	$\log(gf)$
	$\alpha$ Virginis	G238-44		
1083.990	67.3	47.5	0.000	-0.939
1084.580	9.9	60.8	0.006	-0.587
1085.546		40.2	0.016	-1.079
1085.701	<0.2	55.7	0.016	-0.320

Note. N II absorption in  $\alpha$  Virginis is from ISM material (York & Kinahan 1979).

et al. (2012) and Koester et al. (2014), we compute the diffusion flux of metals through the visible atmosphere of G238-44 to arrive at the chemical composition of the accreting material (column 5 of Table 5).

#### 4.1. Minerals, Metals, and Ices

G238-44 provides detections for many elements. Ni is an important element, but it is not detected. We assume it is present in chondritic ratios to Fe, as they have similar behaviors based on condensation temperatures and tendencies to be in a metallic form.

Referring to the % mass composition column in Table 5, Fe is the most abundant element in the accreting material, comprising nearly half of the total mass. This is already suggestive of a contribution from Fe in metallic form, with a mass percentage greater than that in bulk Earth (29%; Allègre et al. 2001) though not so high as in planet Mercury (69%; Bruger et al. 2018).

This stands in contrast to the substantial abundance of the volatile element N at 0.9% by mass. Such a value is not at all characteristic of rocky planetary bodies that formed interior to the ice line of their host star; e.g., bulk Earth has N by mass of roughly 0.00013% (Allègre et al. 2001). Instead, the N abundance found in the material polluting G238-44 is similar to outer solar system objects such as comet Halley (1.5%; Jessberger et al. 1988) and the exo-Kuiper Belt analog polluting G200-39 (2%; Xu et al. 2017). Such planetary bodies formed well beyond the ice lines in their protoplanetary discs, where the stability of  $N_2$  and ammonia ices allow these compounds to remain incorporated in solids as observed on the surfaces of Pluto and Charon (Cruikshank et al. 2015). It follows that a substantial amount of  $H_2O$  ice is also expected to go along with icy compounds of N and other volatiles such as C and S.

Additionally, it can be seen in Table 5 that the Mg abundance is much higher than Si ( $\sim 4.7$  times by number). In solar system rocks, Mg/Si is usually  $\sim 1$  (e.g., Lodders 2021). We checked this ratio against abundance data from the Hypatia Catalog (Hinkel et al. 2014) and found it unlikely that such a ratio could be explained by nucleosynthetic variability (e.g., Bond et al. 2010; Delgado Mena et al. 2010; Bonsor et al. 2021). The observed abundance is unusual, but it does not change the interpretation given in Section 4.2. If Mg/Si were lower (i.e., “normal”), then it would be even more difficult to describe the data with a single object.

To better assess the mineralogy of the material accreting onto G238-44, we calculate the oxygen budget following Klein et al. (2010). This provides an accounting for accreted O under an initial assumption that all O is tied up in solid planetary system material as rocky mineral oxides (e.g., MgO,  $Al_2O_3$ ,  $SiO_2$ ,  $P_2O_5$ , CaO, FeO or  $Fe_2O_3$ , and NiO; in general, molecules of the form  $Z_{p(Z)}O_{q(Z)}$ ). The oxygen budget  $O_{\text{budget}}$  is defined as

$$O_{\text{budget}} = \sum_Z \frac{q(Z) n(Z)}{p(Z) n(O)}. \quad (1)$$

For a “perfect” rock  $O_{\text{budget}}=1$ , and in the case of a dry rocky parent body, this should be realized when considering only mineral oxides with the major and minor rock-forming elements. If one initially obtains an  $O_{\text{budget}} < 1$  when considering only mineral oxides, then there is an oxygen excess and the additional O atoms are presumed to be associated with ices ( $H_2O$  and possibly CO and  $CO_2$  if sufficient C is present). If an  $O_{\text{budget}} > 1$  is initially obtained, then there is an oxygen deficit and it is assumed that metallic

material (typically Fe) is present as is found within the metal cores of differentiated bodies in our solar system.

Assessing  $O_{\text{budget}}$  for G238-44 using the values given in Table 5 and only the rocky mineral oxides listed above (i.e., no ices or consideration of C or N), we find it to be nearly balanced within the various abundance uncertainties ( $O_{\text{budget}} \simeq 1$ ). However, this leaves the significant contribution from C and N to the parent body ( $\approx 4.4\%$  by mass) unaccounted for. Carbon and nitrogen can be locked within organic materials that are found in trace amounts in solar system bodies, and indeed are the most abundant C- and N-bearing phase within carbonaceous chondrites (e.g., Pearson et al. 2006). The C and N in G238-44 could be present as aromatic organic compounds composed only of C, N, and H (e.g., Pyrrole, Aniline, Pyrazine, Purine, etc.). However, such a parent body would be very unusual, effectively a rock marbled with organic substances. Lacking a reasonable analog to such a parent body within the solar system, we opt instead for the C and N to be in the more familiar form of ices.

As noted earlier, the presence of C- and N-bearing ices heralds the presence of icy  $\text{H}_2\text{O}$ .  $\text{H}_2\text{O}$ , CO, and  $\text{CO}_2$  ices will “steal” O away from rocky minerals, thus leading to deficit conditions, meaning the inclusion of ices can only be balanced by allowing for metallic material. Again, a single body hosting significant quantities of icy material—especially C- and N-bearing ices—and metallic Fe would be unlike anything currently known within the solar system. Even the EH chondrites—primitive rocks rich in Fe, candidates for the composition of an early Earth (Javoy et al. 2010)—are a poor description of the data.

To explain what appears to be the simultaneous existence of significant icy and metallic portions in the material being accreted by G238-44, we propose the presence of two distinct parent bodies, one core-like and one volatile-rich. Below, we motivate such a scenario with the help of literature studies and explore what two parent bodies would be capable of producing the observed abundances in G238-44.

#### 4.2. Simultaneous Accretion from Two Parent Bodies

The material accreting onto G238-44 has two opposing characteristics:

1. Significant Portion of Iron in Metallic Form. Fe metal indicates a core-like structure of a differentiated body, likely forming near its host star as an asteroid or terrestrial planet (Trønnes et al. 2019).
2. High Concentration of Nitrogen. A large N abundance indicates formation far from the host star, well beyond the ice line, as in Kuiper Belt objects (Bierson & Nimmo 2019). Such minor planets are rich in ices of N, C, and O.

The characteristics of the material polluting the atmosphere of G238-44 suggest that it originated from two distinct formation locations of the host stars’ planetary system. We invoke a model wherein there are two compositionally distinct parent bodies simultaneously polluting G238-44, one coming from the inner planetary system (e.g., an asteroid-like body) and the other coming from the outer planetary system (e.g., a Kuiper Belt object analog).

Literature works have laid the foundation for such an interpretation, suggesting that not only is it possible to have two bodies simultaneously polluting a white dwarf atmosphere

but that for smaller bodies it may be common. Jura (2008) first proposed multiple bodies being captured around a white dwarf to explain “invisible” accretion reservoirs (like the one around G238-44). In their model, a second body approaching a WD has a trajectory that is inclined to an existing accretion disk of an earlier tidally disrupted body, which results in an impact that causes grains from both objects to vaporize due to sputtering. The disk is then mainly composed of gas with an infrared excess that would be difficult to detect.

Recent works have consistently indicated that a continuous stream of smaller bodies should be arriving at the white dwarf star (e.g., Wyatt et al. 2014; Turner & Wyatt 2020; Li et al. 2022; Trierweiler et al. 2022, and references therein). The work of Li et al. (2022) is especially relevant in this context, as it explores (for the solar system) the transport of main-belt asteroids and trans-Neptunian objects (or Kuiper Belt objects) to a white dwarf as a function of time. Specifically, they find it is possible to deliver both a main-belt asteroid and Kuiper Belt object to the central white dwarf star within a white dwarf cooling time of 100 Myr. Events involving an inner planetary system body and outer planetary system body are rare, though, as Kuiper Belt object pollution is supposed to increase in frequency for cooling times  $\gtrsim 100$  Myr (Li et al. 2022). This would be consistent with G238-44 being the first white dwarf we know of to possibly be experiencing a simultaneous pollution event of such type.

The results from theoretical and simulation work to date support the possibility of having two bodies from distinct formation locations around G238-44 now simultaneously polluting the white dwarf star. Next, we must verify that a two-body model is capable of producing a reasonable fit to the abundance data.

In arriving at a two-body fit to the data, we envision a metallic parent body with mass comparable to an asteroid but with composition similar to Mercury (Brugger et al. 2018; Nittler et al. 2018). This choice is made as Mercury is the best-characterized metal-dominated body we know of in the solar system. The asteroid 16 Psyche may be a more appropriate analogy, based on the fact that it is the largest M-type (metal-rich) asteroid known, but it lacks detailed elemental composition estimates (the Psyche asteroid mission will launch in the future to better characterize this interesting object). As a model for the icy body, we adopt the observed abundances of the extrasolar Kuiper Belt object-analog G200-39 (Xu et al. 2017). This measurement is more relevant than in situ measurements of comets because it fully captures the bulk composition, which in the case of a Kuiper Belt object is likely unchanged since its formation. Recent measurements of comet dust (e.g., Jessberger et al. 1988; Bardyn et al. 2017) do not account for the entire body, and short-period comets have had their volatile compositions altered significantly by their multiple passes close to the Sun. Pluto, which is expected to be a core made up of hydrated rock covered by an ice-rich mantle and crust (McKinnon et al. 2017), could be a relevant icy body analog but is not characterized well at an elemental level.

In utilizing the parent body polluting G200-39 as a reference for our icy body abundances, we revisited its water-ice fraction. Accounting for CO as well as mineral oxides, we arrive at a somewhat different result than that quoted in Xu et al. (2017). We find that 65% of the O is excess, corresponding to a water fraction of 46% by mass. By number, the ratio of excess O atoms to N is 19.7, and the ratio of excess O to C is 3.4. These

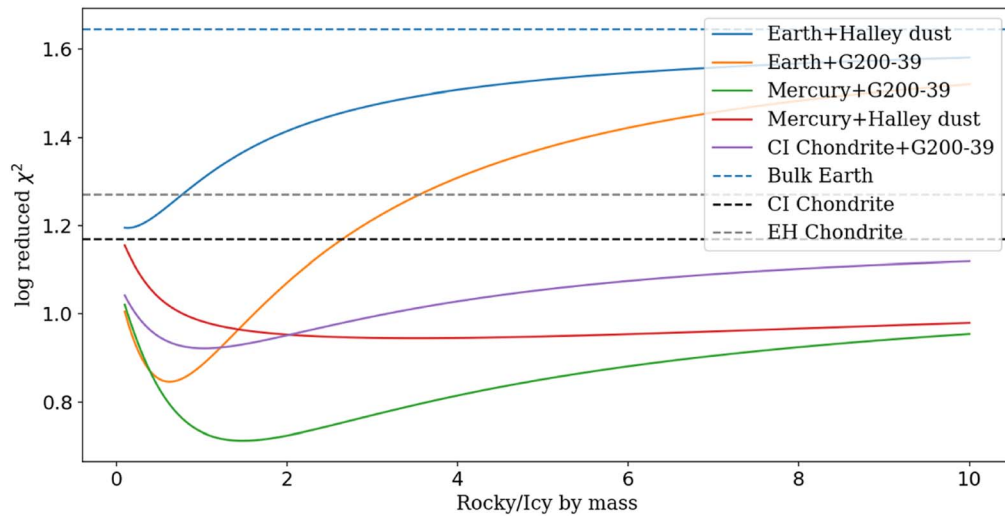


**Figure 7.** Reduced  $\chi^2$  fits exploring two-body models; note that the y-axis is  $\log_{10}$ . Only atomic abundance information is incorporated into these model tests; i.e., the presence of metallic and icy material is not assessed by the  $\chi^2$  fit. We find that a mix of metal-dominated Mercury-like material and icy Kuiper Belt object-like material (G200-39; see text) in a ratio of 1.7:1 provides the best fit to the data.

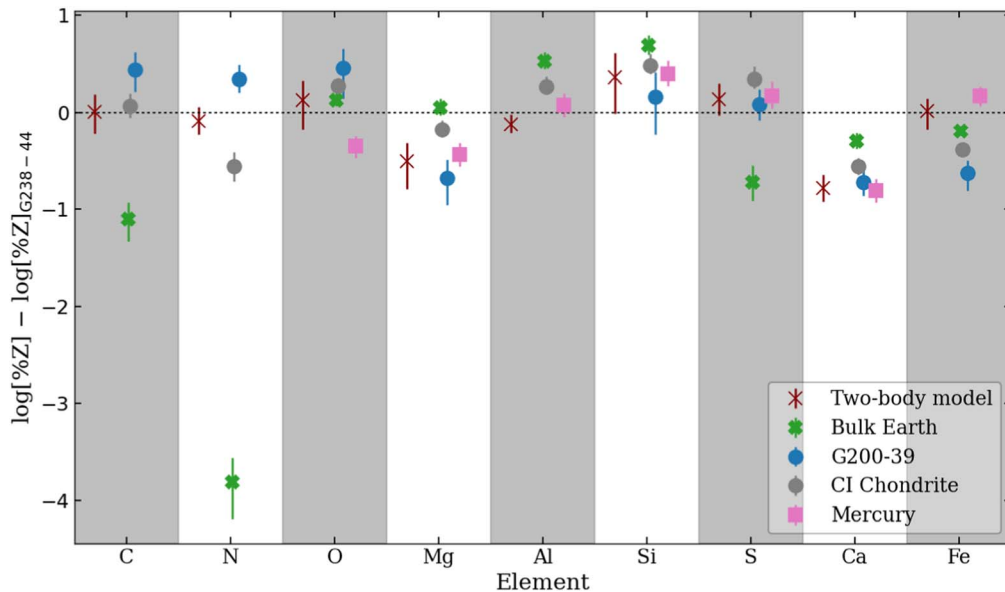


**Figure 8.** Residuals for elemental abundances (expressed as a percentage of the total parent body mass) when comparing G238-44 and various parent body models. The two-body model, informed from the best fit in Figure 7 and discussed in Section 4.2, fits within the errors both for Fe and ices (C, N, and O). Single-body models are not reasonable matches to the data.

numbers are roughly consistent with measurements of solar system comets (Mumma & Charnley 2011).

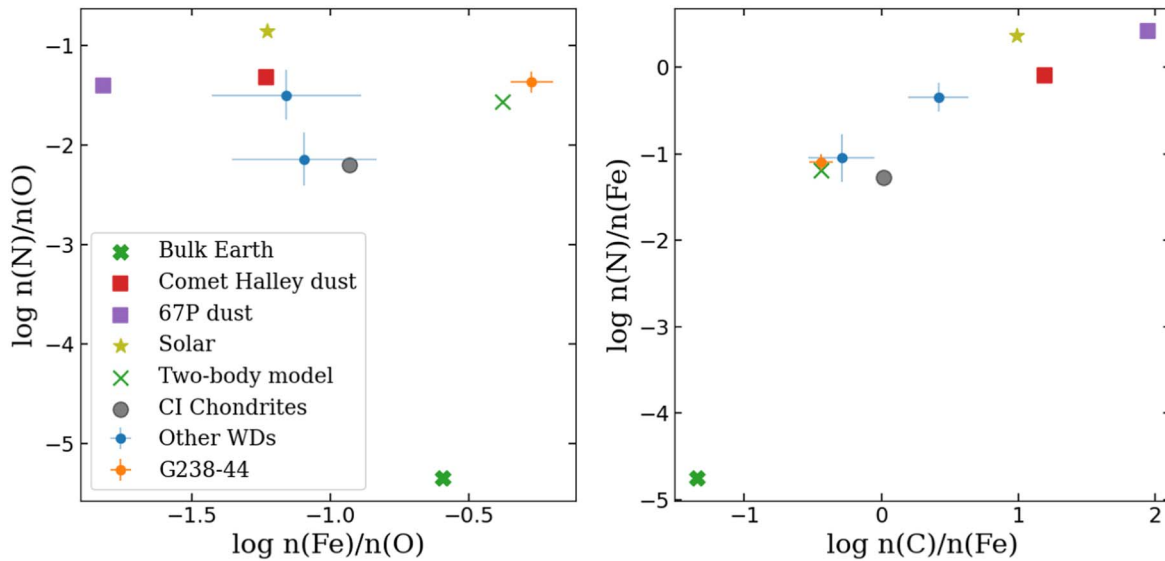
Figures 7 and 8 explore  $\chi^2$  minimization for a variety of different two-body models (and reference single-body models). We allowed the relative mass fraction of rocky-metal to icy material to vary, and we fit against all measured elemental abundances. The Mercury+G200-39 model significantly outperforms all other models, especially for a 1.7:1 mix of Mercury-like and icy Kuiper Belt object-like material.

Figure 9 shows how this particular model produces C/N/O/Fe abundance ratios that are in good agreement with measurements for G238-44 and yet distinct from other solar system bodies.

We are thus able to identify a mix of two parent bodies that reproduces the observed pollution pattern in the atmosphere of G238-44. Based on the elemental diffusion fluxes in column 6

of Table 5, we can make an estimate of how big each of these distinct parent bodies may have been.

In aggregate, G238-44 hosts a total mass accretion rate of  $5.8 \times 10^7 \text{ g s}^{-1}$ . The star has been known to have pollution in its atmosphere since its first high-dispersion IUE observation in 1982. Assuming constant accretion over the past 40 yr, the star has swallowed  $7 \times 10^{16} \text{ g}$ . However, we do not know how long it has been since the currently observed accretion began nor how long it will continue forward. We can get an idea of a range of the total mass of the parent bodies using previous estimates for WD disk lifetimes of between 0.03 and 5 Myr (Girven et al. 2012). Taking the simplifying assumption that the observed accretion rate is representative of a time-averaged mean accretion rate over the disk lifetime, we arrive at a total pollution mass roughly between  $6 \times 10^{19}$  and  $9 \times 10^{21} \text{ g}$ . Taking now the 1.7:1 mass ratio of rocky-metal to icy material, we arrive at a metal-rich body mass of between  $3.8 \times 10^{19}$  and



**Figure 9.** Elemental abundance ratios by number for the material polluting G238-44 compared to other WDs, solar system bodies, and the two-body model we propose in Section 4.2. Abundances from: Bulk Earth—Allègre et al. (2001), Mercury—Brugger et al. (2018); Nittler et al. (2018), Comet Halley dust—Jessberger et al. (1988), 67P/ChuryumovGerasimenko—Bardyn et al. (2017), Solar & CI Chondrite—Lodders (2021), G200-39—Xu et al. (2017), GD 378—Klein et al. (2021). O is an incredibly versatile element when it comes to planet formation. It is a significant component of any solar system object. However, C, N, and Fe are much more specialized. Fe abundance is high in objects that formed close to their parent star. In contrast, N can only form in significant amounts past the ice line. We do not expect objects that are high in Fe to also be high in N. G238-44 breaks this trend and has both high Fe/O and N/O. The proposed two-body model is capable of reproducing this unusual characteristic.

$5.7 \times 10^{21}$  g and an icy body mass of between  $2.2 \times 10^{19}$  and  $3.3 \times 10^{21}$  g. For reference, the mass of asteroid 16 Psyche is roughly  $2.3 \times 10^{22}$  g and the mass of the primary within the trans-Neptunian system 47171 Lempo is roughly  $6.7 \times 10^{21}$  g. The two parent bodies possibly polluting G238-44 would each be roughly an order of magnitude less massive than these solar system objects.

## 5. Conclusions

UV and optical spectroscopic data are used to probe heavy elements in the atmosphere of the warm DA white dwarf G238-44. HIRES observations over a baseline of 24 yr show no robust evidence for variations in the equivalent widths of optical metal absorption lines. With a diffusion timescale of days, we find the accretion rate onto the surface of G238-44 does not vary on a timescale of years. The temperature and brightness of this star make it an optimal candidate for further monitoring to detect any change in accretion rates.

Modeling of the spectra allows us to determine the abundances of heavy elements in the star’s atmosphere, from which we infer the composition of the material that pollutes it. Within the uncertainties, we are able to determine that the parent material is rich in nitrogen and likely contains a significant amount of metallic iron. This mix is unlike that of any known solar system body. We suggest that G238-44 is simultaneously accreting a metal-rich exo-planetesimal and a volatile-rich exo-Kuiper Belt object. If our interpretation is correct, this would be the first evidence of simultaneous accretion of two distinct parent bodies in a white dwarf.

The proposed two-body pollution interpretation may explain G238-44’s lack of infrared excess (Jura 2008). While such events are predicted in dynamical simulation work (e.g., Li et al. 2022), they should be very rare for a white dwarf with cooling age  $< 100$  Myr like G238-44. This could be suggestive of a planetary system architecture for G238-44 different from

the solar system, the likes of which allowed the rapid and dramatic perturbation of inner and outer planetesimal populations around G238-44.

We are grateful to K. Long and B. Gänsicke for providing their reduced and combined version of the FUSE spectrum. We are also grateful for helpful advice and conversations with Alexandra Doyle, Isabella Trierweiler, and Edward Young.

This work has been supported by grants from NASA and the NSF to UCLA. T.J. acknowledges support from the UCLA Physics and Astronomy summer 2020 REU program and 2021-22 URSP scholarship. B.K. acknowledges support from the NASA Exoplanets program award number 80NSSC20K0270 (PI Ed D. Young). C.M. and B.Z. acknowledge support from NSF grants SPG-1826583 and SPG-1826550.

This research has made use of the Keck Observatory Archive (KOA), which is operated by the W.M. Keck Observatory and the NASA Exoplanet Science Institute (NExScI).

This research has made use of SIMBAD, SAO/NASA ADS, the Montreal White Dwarf Database, MAST, VALD, NIST, and Kurucz Atomic Line databases, IRAF, Python, and Matplotlib.

Some of the data presented in this work were obtained at the W.M. Keck Observatory, which is operated as a scientific partnership among the California Institute of Technology, the University of California, and the National Aeronautics and Space Administration. The Observatory was made possible by the generous financial support of the W.M. Keck Foundation. We recognize and acknowledge the very significant cultural role and reverence that the summit of Maunakea has always had within the indigenous Hawaiian community. We are most fortunate to have the opportunity to conduct observations from this mountain. We thank the Keck Observatory staff for their dedicated work and support.

*Facilities:* FUSE, HST (STIS, COS), Keck I (HIRES)

## ORCID iDs

Ted M Johnson  <https://orcid.org/0000-0002-1570-2203>  
 Beth L. Klein  <https://orcid.org/0000-0001-5854-675X>  
 D. Koester  <https://orcid.org/0000-0002-6164-6978>  
 Carl Melis  <https://orcid.org/0000-0001-9834-7579>  
 B. Zuckerman  <https://orcid.org/0000-0001-6809-3045>

## References

- Allègre, C., Manhès, G., & Lewin, É. 2001, *E&PSL*, **185**, 49  
 Bardyn, A., Baklouti, D., Cottin, H., et al. 2017, *MNRAS*, **469**, S712  
 Barstow, M. A., Barstow, J. K., Casewell, S. L., Holberg, J. B., & Hubeny, I. 2014, *MNRAS*, **440**, 1607  
 Bierson, C. J., & Nimmo, F. 2019, *Icar*, **326**, 10  
 Bond, J. C., O'Brien, D. P., & Lauretta, D. S. 2010, *ApJ*, **715**, 1050  
 Bonsor, A., Jofré, P., Shorttle, O., et al. 2021, *MNRAS*, **503**, 1877  
 Brugger, B., Mousis, O., Deleuil, M., & Ronnet, T. 2018, *EPSC*, **12**, EPSC2018-404  
 Chayer, P., Vennes, S., Pradhan, A. K., et al. 1995, *ApJ*, **454**, 429  
 Cruikshank, D. P., Grundy, W. M., DeMeo, F. E., et al. 2015, *Icar*, **246**, 82  
 Cunningham, T., Tremblay, P.-E., Bauer, E. B., et al. 2021, *MNRAS*, **503**, 1646  
 Debes, J. H., & López-Morales, M. 2008, *ApJL*, **677**, L43  
 Debes, J. H., & Sigurdsson, S. 2002, *ApJ*, **572**, 556  
 Delgado Mena, E., Israelian, G., González Hernández, J. I., et al. 2010, *ApJ*, **725**, 2349  
 Doyle, A. E., Desch, S. J., & Young, E. D. 2021, *ApJL*, **907**, L35  
 Doyle, A. E., Young, E. D., Klein, B., Zuckerman, B., & Schlichting, H. E. 2019, *Sci*, **366**, 356  
 Dufour, P., Blouin, S., Coutu, S., et al. 2017, in ASP Conf. Ser. 509, 20th European White Dwarf Workshop, ed. P. E. Tremblay, B. Gänsicke, & T. Marsh (San Francisco, CA: ASP), 3  
 Dupuis, J., Bouabid, M. P., Wesemael, F., & Chayer, P. 2007, in ASP Conf. Ser. 372, 15th European Workshop on White Dwarfs, ed. R. Napiwotzki & M. R. Burleigh (San Francisco, CA: ASP), 261  
 Dupuis, J., Chayer, P., & Hénault-Brunet, V. 2010, in AIP Conf. Ser. 1273, 17th European White Dwarf Workshop, ed. K. Werner & T. Rauch (Melville, NY: AIP), 412  
 Farihi, J. 2016, *NewAR*, **71**, 9  
 Farihi, J., Gänsicke, B. T., & Koester, D. 2013, *Sci*, **342**, 218  
 Farihi, J., Jura, M., & Zuckerman, B. 2009, *ApJ*, **694**, 805  
 Farihi, J., van Lieshout, R., Cauley, P. W., et al. 2018, *MNRAS*, **481**, 2601  
 Gänsicke, B. T., Koester, D., Farihi, J., et al. 2012, *MNRAS*, **424**, 333  
 Gänsicke, B. T., Schreiber, M. R., Toloza, O., et al. 2019, *Natur*, **576**, 61  
 Girven, J., Brinkworth, C. S., Farihi, J., et al. 2012, *ApJ*, **749**, 154  
 Hébrard, G., Allard, N. F., Kielkopf, J. F., et al. 2003, *A&A*, **405**, 1153  
 Hinkel, N. R., Timmes, F. X., Young, P. A., Pagano, M. D., & Turnbull, M. C. 2014, *AJ*, **148**, 54  
 Holberg, J. B., Barstow, M. A., & Green, E. M. 1997, *ApJL*, **474**, L127  
 Holberg, J. B., Barstow, M. A., & Sion, E. M. 1998, *ApJS*, **119**, 207  
 Javoy, M., Kaminski, E., Guyot, F., et al. 2010, *E&PSL*, **293**, 259  
 Jessberger, E. K., Christoforidis, A., & Kissel, J. 1988, *Natur*, **332**, 691  
 Jura, M. 2003, *ApJL*, **584**, L91  
 Jura, M. 2006, *ApJ*, **653**, 613  
 Jura, M. 2008, *AJ*, **135**, 1785  
 Jura, M., & Xu, S. 2012, *AJ*, **143**, 6  
 Jura, M., Xu, S., Klein, B., Koester, D., & Zuckerman, B. 2012, *ApJ*, **750**, 69  
 Jura, M., & Young, E. D. 2014, *AREPS*, **42**, 45  
 Klein, B., Jura, M., Koester, D., & Zuckerman, B. 2011, *ApJ*, **741**, 64  
 Klein, B., Jura, M., Koester, D., Zuckerman, B., & Melis, C. 2010, *ApJ*, **709**, 950  
 Klein, B. L., Doyle, A. E., Zuckerman, B., et al. 2021, *ApJ*, **914**, 61  
 Koester, D. 2009, *A&A*, **498**, 517  
 Koester, D. 2010, *MmSAI*, **81**, 921  
 Koester, D., Gänsicke, B. T., & Farihi, J. 2014, *A&A*, **566**, A34  
 Kuiper, G. P. 1942, *ApJ*, **96**, 315  
 Li, D., Mustill, A. J., & Davies, M. B. 2022, *ApJ*, **924**, 61  
 Lodders, K. 2021, *SSRv*, **217**, 44  
 Luyten, W. J. 1945, *Sci*, **101**, 79  
 Malamut, C., Redfield, S., Linsky, J. L., Wood, B. E., & Ayres, T. R. 2014, *ApJ*, **787**, 75  
 McKinnon, W. B., Stern, S. A., Weaver, H. A., et al. 2017, *Icar*, **287**, 2  
 Melis, C., & Dufour, P. 2017, *ApJ*, **834**, 1  
 Melis, C., Farihi, J., Dufour, P., et al. 2011, *ApJ*, **732**, 90  
 Moos, H. W., Cash, W. C., Cowie, L. L., et al. 2000, *ApJL*, **538**, L1  
 Mullally, F., Kilic, M., Reach, W. T., et al. 2007, *ApJS*, **171**, 206  
 Mumma, M. J., & Charnley, S. B. 2011, *ARA&A*, **49**, 471  
 Nittler, L. R., Chabot, N. L., Grove, T. L., & Peplowski, P. N. 2018, in Mercury: The View after MESSENGER, ed. S. C. Solomon, L. R. Nittler, & B. J. Anderson (Cambridge: Cambridge Univ. Press), 30  
 Pearson, V. K., Sephton, M. A., Franchi, I. A., Gibson, J. M., & Gilmour, I. 2006, *M&PS*, **41**, 1899  
 Raddi, R., Gänsicke, B. T., Koester, D., et al. 2015, *MNRAS*, **450**, 2083  
 Rocchetto, M., Farihi, J., Gänsicke, B. T., & Bergfors, C. 2015, *MNRAS*, **449**, 574  
 Science Software Branch at STScI 2012, PyRAF: Python alternative for IRAF, Astrophysics Source Code Library, ascl:1207.011  
 Trierweiler, I. L., Doyle, E. A., Melis, C., Walsh, K., & Young, E. D. 2022, *ApJ*, **936**, 30  
 Trønnes, R., Baron, M., Eigenmann, K., et al. 2019, *Tectp*, **760**, 165  
 Turner, S. G. D., & Wyatt, M. C. 2020, *MNRAS*, **491**, 4672  
 Vennes, S., Thejll, P., & Shipman, H. L. 1991, in White Dwarfs, ed. G. Vauclair & E. Sion (Dordrecht: Kluwer), 235  
 Veras, D. 2021, Oxford Research Encyclopedia of Planetary Science (Oxford: Oxford Univ. Press)  
 Vogt, S. S., Allen, S. L., Bigelow, B. C., et al. 1994, *Proc. SPIE*, **2198**, 362  
 Wilson, D. J., Gänsicke, B. T., Farihi, J., & Koester, D. 2016, *MNRAS*, **459**, 3282  
 Wilson, D. J., Gänsicke, B. T., Koester, D., et al. 2019a, *MNRAS*, **483**, 2941  
 Wilson, T. G., Farihi, J., Gänsicke, B. T., & Swan, A. 2019b, *MNRAS*, **487**, 133  
 Wyatt, M. C., Farihi, J., Pringle, J. E., & Bonsor, A. 2014, *MNRAS*, **439**, 3371  
 Xu, S., Dufour, P., Klein, B., et al. 2019, *AJ*, **158**, 242  
 Xu, S., Zuckerman, B., Dufour, P., et al. 2017, *ApJL*, **836**, L7  
 York, D. G., & Kinahan, B. F. 1979, *ApJ*, **228**, 127  
 Zuckerman, B., Koester, D., Dufour, P., et al. 2011, *ApJ*, **739**, 101  
 Zuckerman, B., Koester, D., Reid, I. N., & Hüsch, M. 2003, *ApJ*, **596**, 477  
 Zuckerman, B., & Reid, I. N. 1998, *ApJL*, **505**, L143  
 Zuckerman, B., & Young, E. D. 2018, in Handbook of Exoplanets, ed. H. J. Deeg & J. A. Belmonte (Cham: Springer), 14